



Experimental Study on the Full-Field Characteristics of Displacements of a Bedded Limestone by Digital Image Correlation

Yang-Yi Zhou · Xu-Feng Liu · Yan-Hua Gong · Guo-Qiang Zhu

Received: 27 May 2020 / Accepted: 19 November 2020 / Published online: 25 November 2020
© Springer Nature Switzerland AG 2020

Abstract Rocks with bedding or foliation usually behave as anisotropic body. Understanding the full-field displacement characteristics of anisotropic rocks is of particular interest, since the behaviors of anisotropic rocks vary with the angle between bedding and loading direction, and are thus more difficult to predict than isotropic rocks. By the digital image correlation technique, the two-dimensional displacement fields of a bedded limestone with different bedding angles are obtained in this paper. Displacement field evolution process with loading is described in detail, in which the progressive rotation of principal strains can be identified. The displacement field pattern also varies with loading angle. If some threshold of loading angle is surpassed, the pattern can transit from one to another, which is essentially determined by the tensor transformation rule of compliance matrix. The non-coaxiality between

principal strains and stresses with respect to different loading angles are calculated from both test results and numerical simulation, which further confirms the validity of transverse isotropy—a fundamental assumption for rocks exhibiting layered structure.

Keywords Anisotropic rock · Full-field displacement · Digital image correlation · Principal strain · Non-coaxiality

1 Introduction

As natural material with geological origin, rocks in most cases cannot be treated as ideally isotropic body, due to certain mineral composition and arrangement pattern. In other words, the deformation and strength characteristics of rocks often exhibit different degrees of anisotropy. For example, the genesis of sedimentary rocks usually brings about bedding structure, which illustrates as layered or lamellar arrangements of material (minerals or larger fragments) at different scales. As a result, more prominent deformation can often be observed perpendicular to bedding. Besides, fracturing along certain paths and the corresponding strength anisotropy can be associated with various kinds of metamorphic rocks, in which the directional distributions of minerals such as foliation, schistosity, cleavage, etc., are generally developed. Deeper

Y.-Y. Zhou (✉) · X.-F. Liu · Y.-H. Gong
Key Laboratory of Ministry of Education on Safe Mining
of Deep Metal Mines, Northeastern University,
Shenyang 110819, Liaoning, China
e-mail: zhouyangyi@mail.neu.edu.cn

G.-Q. Zhu
State Key Laboratory of Geomechanics and Geotechnical
Engineering, Institute of Rock and Soil Mechanics,
Chinese Academy of Sciences, Wuhan 430071, China

G.-Q. Zhu
University of Chinese Academy of Sciences,
Beijing 100049, China

understanding of the mechanical properties of rocks can be gained by investigating the anisotropy of rocks with layered features. Behaviors of layered rock masses around large-scale underground openings can also be more reasonably predicted once rock anisotropy is better understood.

Recent experimental studies on the anisotropic rocks mainly focus on characterizing basic mechanical parameters using simple loading methods. Special attention is paid to the relationship between deformation or strength and loading angle β , which is defined as the angle between normal vector of the internal structure with preferred orientation, such as bedding or foliation, and major loading direction. Common testing methods include uniaxial compression (Hakala et al. 2007; Cho et al. 2012), conventional triaxial compression (McLamore and Gray 1967; Fjær and Nes 2014) and Brazilian splitting (Tavallali and Vervoort 2010; Tan et al. 2015). These studies reveal, from different perspectives, the anisotropic mechanical properties of different rocks. However, only macroscopic equivalent parameters and stress–strain relationship of intact rock samples were obtained from these tests, the detailed full-field characteristics of displacements for anisotropic rocks still remain unclear. As is well known, inhomogeneous and loading angle related deformation pattern are more commonly seen while testing anisotropic rocks even under simple loading conditions. A thorough investigation upon the full-field characteristics of displacements for anisotropic rocks, particularly with respect to different loading angles, is therefore needed to enrich the knowledge about rocks of this type. Since the assumption of transversely isotropy is a common practice for bedded rocks, and nearly all the proposed constitutive equations for bedded rock are based on this assumption, it should be verified by carefully examining the difference between theoretical prediction and experimental result. However, only a few direct experimental evidences support this assumption at present.

Among the various techniques of capturing the displacement field commonly used in material sciences, the digital image correlation (DIC) technique (Sutton et al. 2009) is one of the universally adaptable methods that are acceptably accurate meanwhile easy to implement. Extensive research have shown that the accuracy of displacements measured by DIC depends mainly on the sample shape, resolution

of images and setting of DIC algorithms (Schreier and Sutton 2002; Sutton et al. 2008; Pan et al. 2009; Lee et al. 2011; Hoult et al. 2013). After establishing a sound theoretical basis for the DIC technique, numerous tests using this innovative technique have been carried out to measure the displacements and strains of materials of different kinds, including metal, concrete and rock (Choi and Shah 1997; Wattrisse et al. 2001; Corr et al. 2007; Leplay et al. 2011; Wu et al. 2011; Zhang et al. 2012; Dai et al. 2013; Dutton et al. 2013; Song et al. 2013a, b; Stirling et al. 2013; Alam et al. 2015), and across various scales from nanoscale right up to macroscale (Chang et al. 2005; Berfield et al. 2007). Of particular interest is the characterization of the crack initiation and propagation process of rocks captured by high-speed camera (Ma et al. 2011; Song et al. 2013a, b), sometimes under the condition of pre-existing cracks or holes (Nguyen et al. 2011; Lin and Labuz 2013; Li et al. 2017). Two-dimensional DIC technique is also directly applied to obtain the global or local deformation evolution process of rock samples (Lenoir et al. 2007; Louis et al. 2007; Dautriat et al. 2011; Tudisco et al. 2015; Munoz et al. 2016). Among these experimental investigations using DIC technique, however, the ones specifically designed and applied to anisotropic rocks are seldom reported.

Several questions arise concerning the deformation pattern of anisotropic rocks. For example, how does the deformation pattern vary with the loading angle? How is the non-coaxiality between principal strain and principal stress affected by the internal structure? Whether the experimental results are consistent with predictions based on the transversely isotropy assumption? And in what cases the rocks with lamellar structure could be regarded as transversely isotropic body? In this paper we aim at exploring experimentally the two-dimensional full-field characteristics of displacements for a bedded limestone, by an image acquisition system and verified DIC algorithm. First thin plate samples with different loading angles are prepared to realize quasi-two-dimensional loading or plane stress condition, in which the deformation along the thickness direction could be neglected. Next the surface images during uniaxial loading are continuously recorded by a high-resolution camera. Finally the captured images are analyzed by an open source DIC software to generate the displacement and strain field images, as well as the principal strain vectors. Then the angle relationship between principal strain

and principal stress for ideal transversely isotropic body is obtained by numerical simulation. The assumption of transverse isotropy for bedded rocks is verified by comparing numerical simulation results and experimental results. The above-mentioned questions are then discussed in detail.

2 Test Sample and Configuration

2.1 Sample

The rock used in this study is a limestone which exhibits clear bedding structure (Fig. 1). Dark traces within this gray rock indicate bedding direction. Thickness of a single bed varies between 1 and 2 mm. Mineral composition of this rock is calcite ($\sim 90\%$), quartz ($\sim 8\%$), and sericite ($\sim 2\%$). Average size of the main particles is within 0.04–0.08 mm. The internal planes of weakness are mainly comprised of the flaky minerals (sericite), which is distributed in a narrow band and oriented parallel to bedding. Possible source of anisotropy of this rock may be attributed to the bedding structure as well as the parallel planes of



Fig. 1 Bedded limestone. The dark lines indicate the direction of bedding

weakness. Details of this rock can be found in the reference (Zhou et al. 2016).

2.2 Sample Preparation

The dimension of a standard specimen is 40 mm \times 20 mm \times 5 mm (length \times width \times thickness), in order to meet the requirement of quasi-two-dimensional loading condition. Traditional cutting by metal circular saw is not appropriate for this size since 5 mm thickness is generally at the same level of the saw thickness. A diamond wire cutting apparatus is thus used to prepare this thin specimen. The diameter of a diamond wire is only about 0.35 mm, which is suitable for cutting thin slice and also induces negligible disturbance. Besides, the sample stage can be rotated 360°, thus reducing the difficulty of preparing samples with different loading angles. Since the bedding structure of the rock is relatively stable, the possible influence of sample discreteness can be minimized by carefully choosing the cutting position and cutting angle, namely, the positions that show the minimum variation of bedding are chosen as cutting positions.

A cylindrical core or blocks of other shapes can be adopted. First the block is cut into slices of about 5 mm thick meanwhile ensuring that the bedding is perpendicular to the slice as shown in Fig. 2. A 40 mm \times 20 mm rectangle is then cut from the slice by rotating the stage relative to the wire with an appropriate angle, which is predetermined by the loading angle from 0° to 90°. Grinding of each surface is realized by a small grinding machine. The final samples ready for testing is shown in Fig. 3.

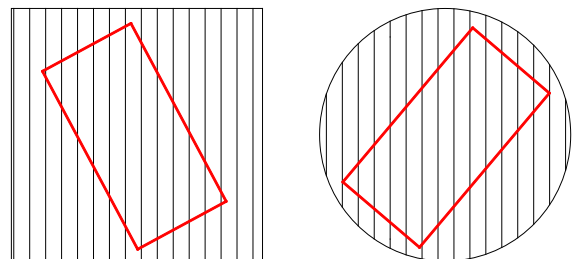


Fig. 2 Method of preparing samples of different loading angles from rectangular or circular samples

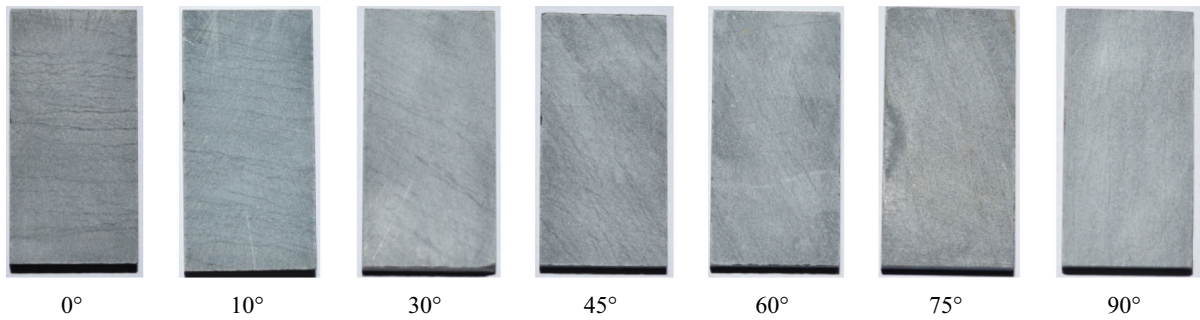


Fig. 3 Samples with different loading angles

2.3 Testing Apparatuses

The uniaxial loading system adopts HUMBOLDT 5030 electronic servo material testing machine, whose maximum loading capacity is 50 kN. The image acquisition system consists of a high-resolution CCD camera, a bilateral telecentric lens, a horizontal lens bench, and a coaxial light source. The CCD camera has a maximum resolution of 4896×3264 pixels (roughly 16 megapixels), a maximum 5 frames per second, and a maximum pixel of $5.5 \mu\text{m}$. The bilateral telecentric lens has a magnification of 0.38, an object distance of 263 mm, an aperture of 16, very low telecentricity ($\text{max} < 0.06^\circ$) and distortion ($\text{max} < 0.08\%$), a wide field depth of 9 mm. The main feature of this lens is that no variation of magnification within the range of field depth, which reduces the possible error induced by the deformation along the thickness direction. The lens bench allows fixation of the lens horizontally. The relative position of the lens and the object is adjusted precisely by the lifting platform and linear guide. The coaxial light source has an emitting area of $100 \times 100 \text{ mm}^2$ and a high brightness, providing uniform and coaxial illumination.

The whole testing system is shown in Fig. 4. Before testing the front surface of the sample is spayed first with a white paint forming background color and then with a black paint forming random speckle pattern. The sample is then placed onto the loading machine and preloaded with a nonzero axial loading. Uniaxial loading is applied along the long axis of the specimen (Fig. 5) under the loading rate of 0.02 mm/min. The image acquisition system is placed in front of the sample, with the optical path perpendicular to the sample surface. The front surface images is continuously captured by the CCD camera in the whole

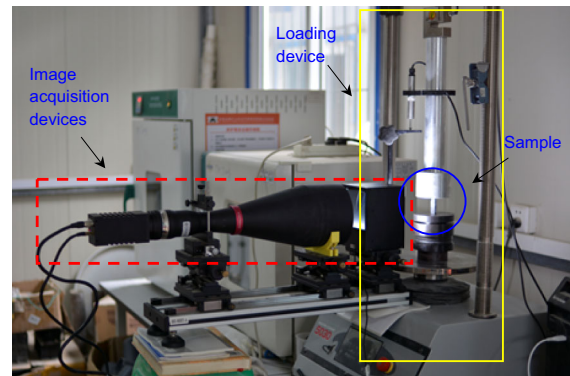


Fig. 4 Testing setup. The loading device is a HUMBOLDT 5030 electronic servo material testing machine with 50 kN loading capacity, the image acquisition devices include a high-resolution CCD camera, a bilateral telecentric lens, a horizontal lens bench, and a coaxial light source

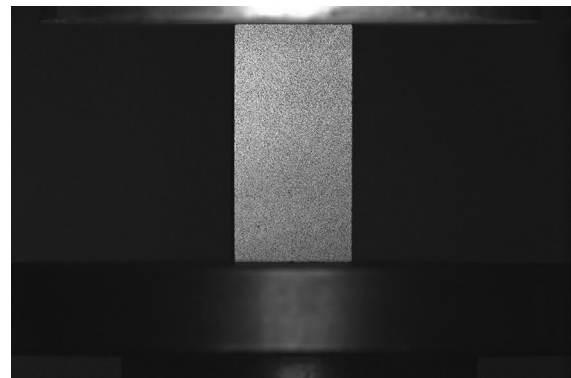


Fig. 5 The speckle pattern and loading setup

process until the peak strength is reached. Vertical displacement of the specimen is independently recorded by a LVDT sensor. The images with specific speckle pattern at different moments are then analyzed using DIC algorithm so as to obtain the 2D full-field characteristics of displacements and strains.

2.4 DIC Technique

The DIC technique offers a convenient and reliable way of obtaining the displacement and strain distributions within a specific area or volume of an object despite of the scale. The fundamental idea behind this algorithm is to find and establish the correlation between pixels on the reference image at initial state and those on the target deformed images. DIC analysis procedure usually involves partition of the reference image into several subsets formed by a group of pixels, searching for the corresponding subset position in the target image according to their correlation coefficient or other equivalent indices, then calculating the discrete displacement field based on the relative displacement of the subset in the deformed image with respect to the same subset in the reference image. The discrete strain field can be easily obtained by differentiating the displacement field in each subset. The reasonable division of subsets is determined artificially or by some optimal algorithms while considering computational efficiency. The continuously distributed displacement or strain field is generated from the discrete version by some interpolation methods. In this study, the open source Ncorr software based on the MATLAB[®] environment is used to calculate the 2D displacement and strain fields. Details of the DIC algorithm adopted in Ncorr can be found in the reference (Blaber et al. 2015). The principal strain tensor image is generated by the open source Ncorr_post software developed by Václav Nežerka in Czech Technical University in Prague. The DIC parameters used in the analysis are: subset radius = 53, subset spacing = 8, strain radius = 8. Before calculating the displacement field, the real size of the image is calibrated by a ruler. A known distance on the ruler, e.g., 1 mm, is related to the corresponding pixels. Then the number of pixels per unit length is obtained for the subsequent pixel-based calculation of displacements and image size.

3 Testing Results

3.1 2D Displacement Fields at Different Loading Stages for a Single Sample

The evolution of 2D displacement fields during loading for a single specimen is exemplified by the

$\beta = 0^\circ$ case. The load–displacement curve is shown in Fig. 6. The horizontal and vertical displacement fields, and principal strain tensor distribution at different loading moments are shown in Table 1. Two obvious features of the full-field displacement evolution, namely progressive rotation and from disordered to ordered deformation pattern, can be identified from these results. More specifically, at the initial loading stages (a–c), the pre-existing micro-cracks within the sample undergo open-to-closure change. The contour maps of the horizontal and vertical displacements exhibit roughly horizontal and vertical fringe patterns in these stages respectively. During the subsequent loading until peak strength (d–g), the horizontal and vertical displacements gradually rotate obvious angles from their respective initial states. While reaching the peak strength, the contour maps of the horizontal and vertical displacements change into nearly vertical and horizontal fringe patterns, rotating about 90° from earlier loading stages. In addition, the evolution of principal strain tensors during loading indicates that at the initial loading stages (a–c) the principal compressive and tensile strain axes basically form an angle of 45° to the horizontal direction. The subsequent loading process drives the principal strains to an ordered state, which means that the principal compressive strain tends to align with the compressive loading direction, whereas the principal tensile strain tends to be orthogonal to it. This transition is the so-called “from disordered to ordered deformation pattern”. These characteristics demonstrate that displacement and principal strain rotations of different degrees will happen with the increase in the stress level, which elucidates that while approaching the peak strength,

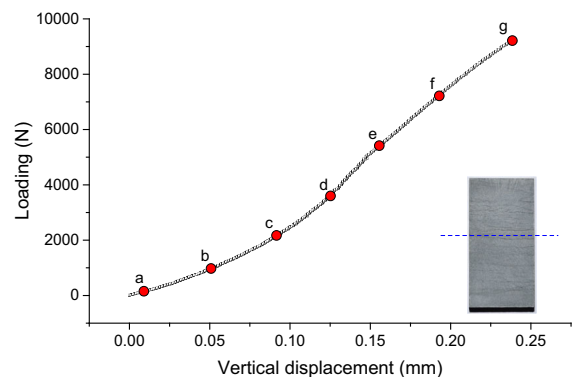
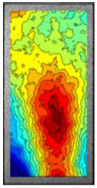


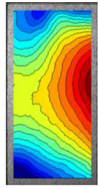




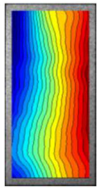
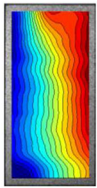




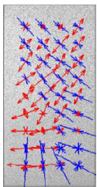
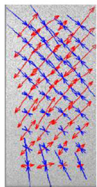
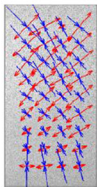
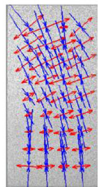
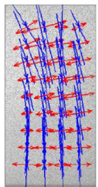
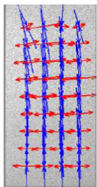
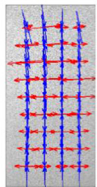


Fig. 6 Loading–displacement curve of $\beta = 0^\circ$ case

Table 1 The displacement fields and principal strains with respect to different loading stages (loading angle $\beta = 0^\circ$)

	a	b	c	d	e	f	g
Horizontal displacement							
Vertical displacement							
Principal strain							

The blue arrow denotes compressive strain, the red arrow denotes tensile strain

the stress plays an outstanding role in the deformation of this bedded limestone.

3.2 2D Displacement Fields at a Specific Moment During Loading for a Single Sample

The 2D displacement fields at a specific moment during loading is demonstrated by the $\beta = 75^\circ$ case. Considering that the load–displacement relationship at the moment denoted by e is within the elastic deformation stage, see Fig. 7, special focus is thus put on the displacements and principal strains (Fig. 8) at this moment. Certain level of inhomogeneity can be observed from the full-field displacements at elastic deformation stage, which is better demonstrated by the curved shape of the contour lines of both the horizontal and vertical displacements. Furthermore, the upper end of the sample is more affected by the non-uniform stresses, due to the specific loading mode of uplifting the lower end meanwhile fixing the upper end, which introduces certain level of end-effect. This effect can also be observed from the contour map of the horizontal displacement field. Although the anti-

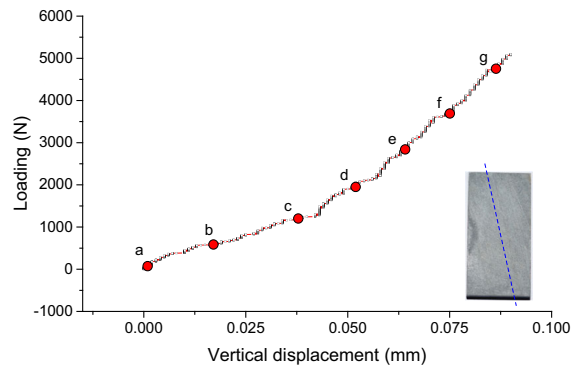


Fig. 7 Loading–displacement curve of $\beta = 75^\circ$ case

friction agent is smeared on both ends to reduce the influence of friction, the end-effect, which exhibits as somewhat distorted contour lines near the upper end, cannot be fully eliminated. The principal strain tensors at upper or lower parts of the sample deviate more or less from the horizontal or vertical directions, while the principal compressive strain at the middle of the sample remains almost vertical. These features reveal that the surface displacement and strain fields of a

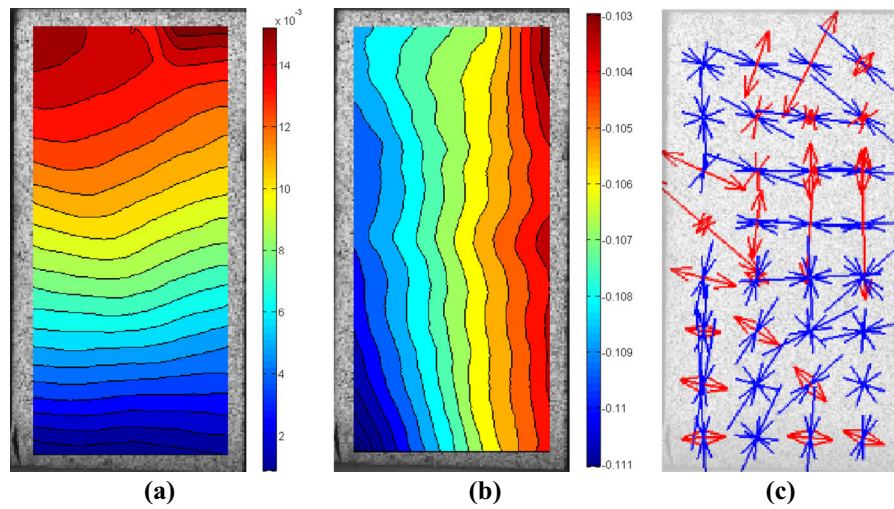


Fig. 8 The displacement fields and principal strains with respect to the loading stage at e point (loading angle $\beta = 75^\circ$, unit: mm). **a** Horizontal displacement, **b** vertical displacement,

c principal strain. The blue arrow denotes compressive strain, the red arrow denotes tensile strain

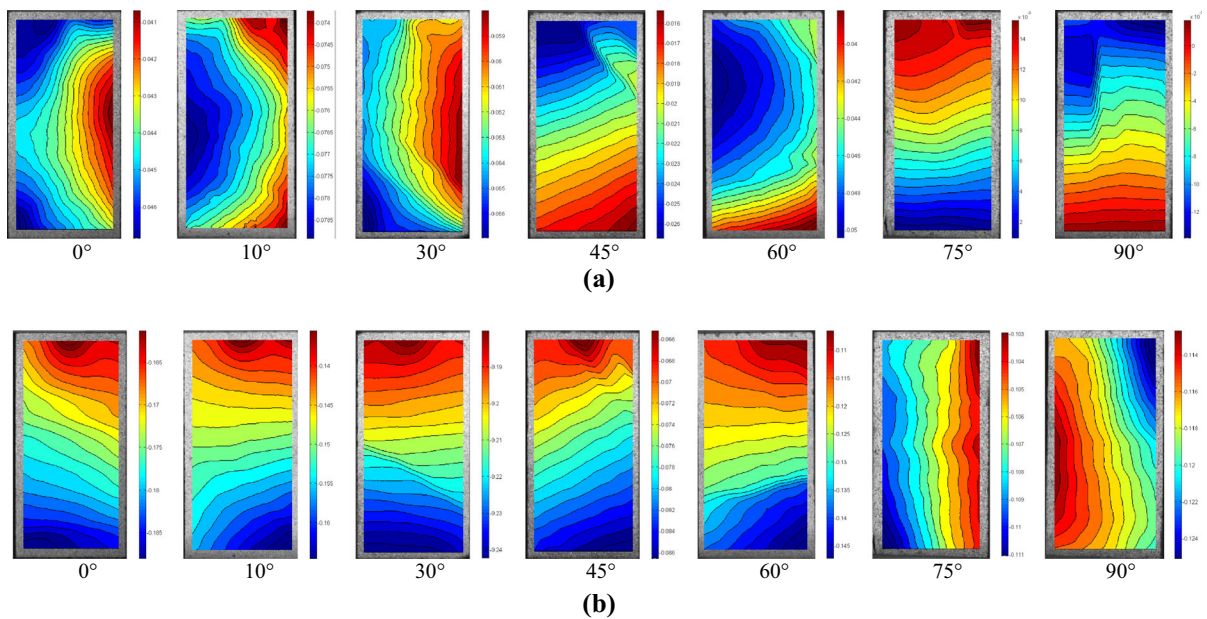


Fig. 9 The displacement fields of samples with different loading angles at elastic deformation stage. **a** Horizontal displacement, **b** vertical displacement, unit: mm

sample usually exhibit non-uniform distribution pattern during loading, which means that the displacement and strains are not the same over the entire surface. It is thus implied that the traditional measurement technique, such as the LVDT, can only obtain the overall equivalent deformation, but cannot reflect local details or variations.

3.3 2D Displacement Fields with Respect to Different Loading Angles

In order to compare the displacement fields with respect to different loading angles under the same stress level, two moments in the loading process, namely the elastic deformation stage (roughly 50% of

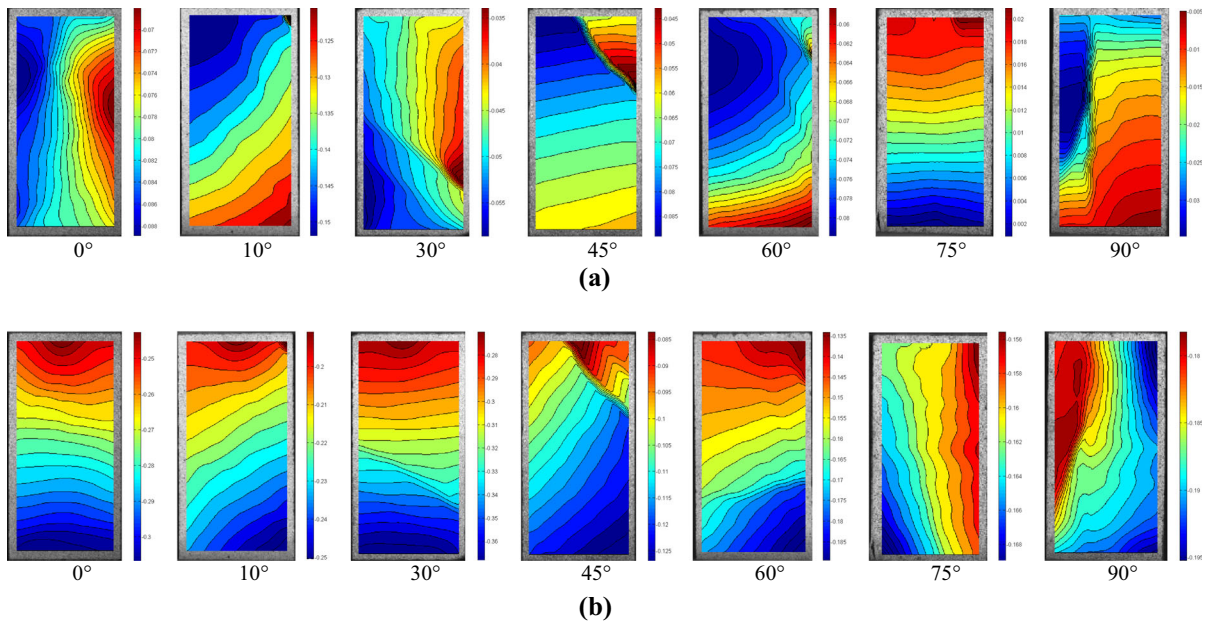


Fig. 10 The displacement fields of samples with different loading angles at near peak strength stage. **a** Horizontal displacement, **b** vertical displacement, unit: mm

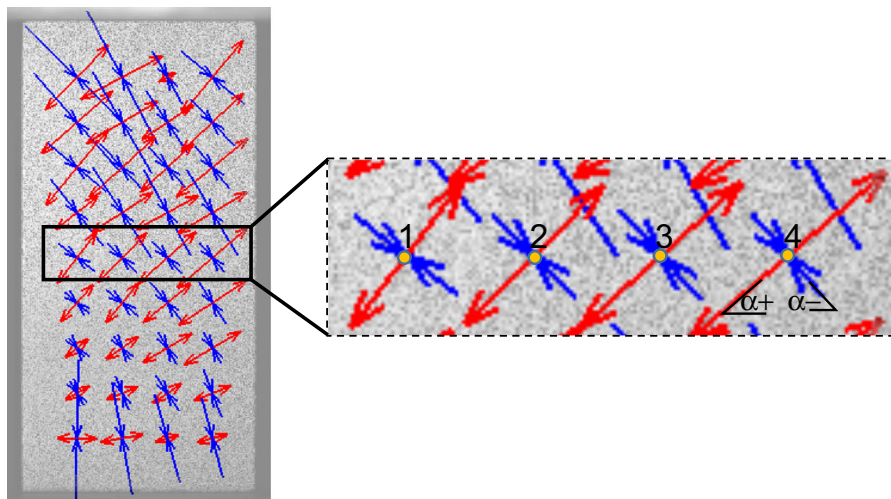


Fig. 11 Principal strain representation and the definition of α angle. The angle α formed by counterclockwise rotating from horizontal direction is defined as positive angle ($\alpha+$), while that by clockwise rotating is defined as negative angle ($\alpha-$). The α

angles of principal tensile strain are measured at points 1–4 in the middle of the sample. Red arrow represents tensile strain, while blue arrow represents compressive strain

the peak strength) and the near-peak stage (right before failure occurs) are chosen and the corresponding horizontal and vertical displacement fields are shown respectively in Figs. 9 and 10 together with their respective loading angles.

From the horizontal displacement field at elastic deformation stage it is clear that when the loading angles are less than 45° , the contour lines form large angles with respect to the horizontal direction, while the opposite trend emerges when the loading angles are larger than 45° , namely the contour lines form

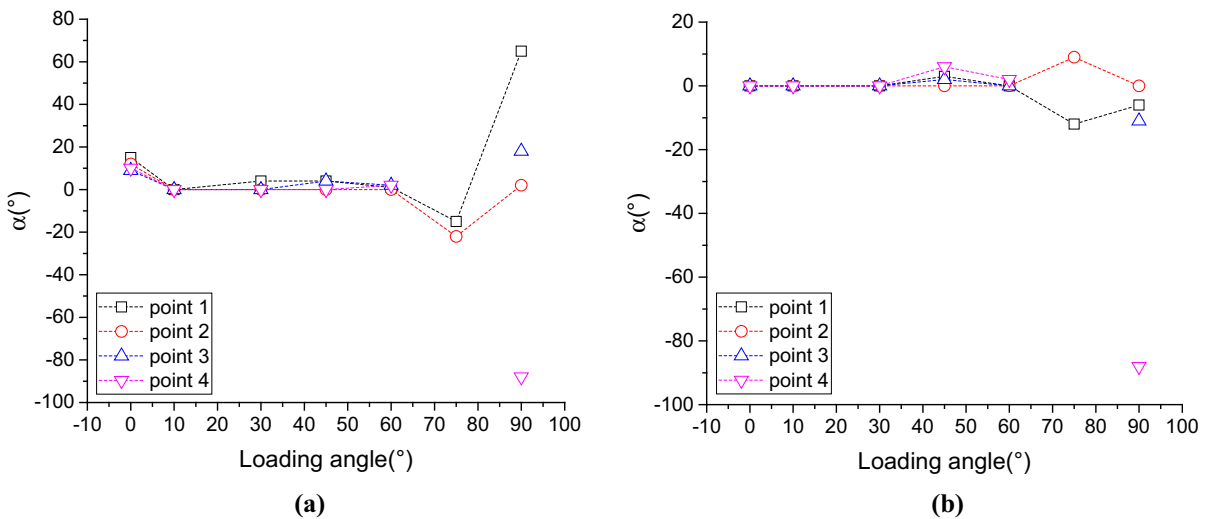


Fig. 12 The α angle of principal tensile strain at different loading stages with respect to different loading angles. **a** elastic deformation stage, **b** near peak strength stage

small angles with or are nearly parallel to the horizontal direction. From the vertical displacement field at elastic deformation stage it can be seen that when the loading angles are less than 60° the contour lines form small angles with or are nearly parallel to the horizontal direction, while they form large angles with or are nearly orthogonal to the horizontal direction when the loading angles are larger than 60° .

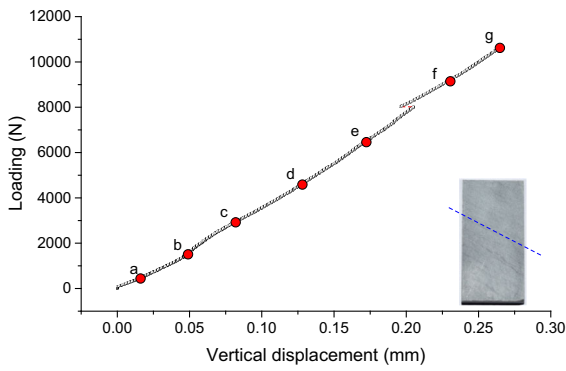
At near-peak stage obvious shear deformations or even cracks have sufficiently developed along its corresponding bedding directions within several samples. This can lead to the distortion of the contour lines at or near the crack and discontinuity of the contour lines across the crack. Cracks can also induce the rotations of the contour lines, particularly for the $\beta = 10^\circ$ and $\beta = 45^\circ$ cases, compared with those at the elastic deformation stage. It is nevertheless found that the general variation trend of the displacement fields with loading angles at both loading stages are consistent.

4 Discussions

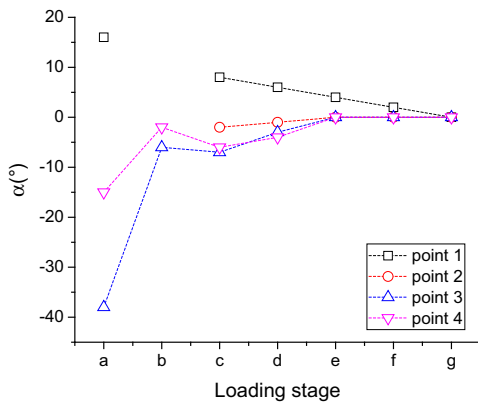
4.1 Relationship Between Principal Strain and Loading Angle

In order to minimize the influence of the end-effect on the results, four sampling positions in the middle of a sample are chosen to measure the corresponding

angles between the principal tensile strain and horizontal direction, as shown in Fig. 11. The α angle formed by counterclockwise rotating from horizontal direction is defined as positive angle, while that by clockwise rotating is defined as negative angle. The α angles of the principal tensile strain at the four positions with respect to different loading angles, corresponding to the elastic deformation stage and the near-peak stage, are shown in Fig. 12. As can be seen, these angles are generally small, most of which are within $\pm 20^\circ$. The principal tensile strain is even roughly oriented horizontally at the elastic deformation stage while the loading angles vary from 10° to 60° . The angles of the principal tensile strain approach -20° at elastic deformation stage, while reducing to about $\pm 10^\circ$ at the near-peak stage in the $\beta = 75^\circ$ case. It is indicated that the directions of the principal strains are affected both by the stress level and by the inherent anisotropy. The influence of stress is more obvious while approaching peak strength. The α angle is approaching 0° no matter what the loading angle is, which indicates that the principal strain axes are progressively driven to the directions of the corresponding principal stresses, whereas at lower stress level (elastic stage) the variation of α angle is more obvious ($\pm 20^\circ$). Similar phenomena can also be found in the $\beta = 90^\circ$ case.



(a)



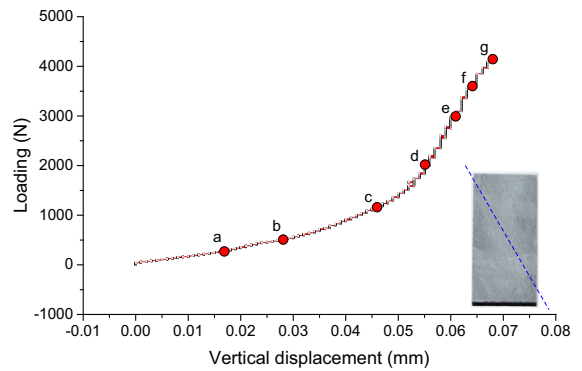
(b)

Fig. 13 The α angle of principal tensile strain at different loading stages with respect to 30° loading angle. **a** loading-displacement curve, **b** α angle at different stages

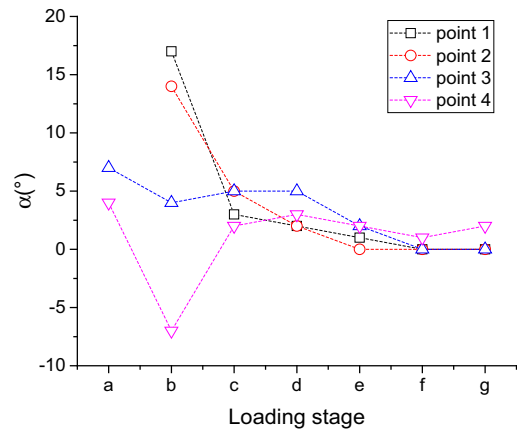
4.2 Relationship Between Principal Strain and Principal Stress

The principal stresses and the corresponding principal strains are not coaxial theoretically for the case of transversely isotropic elastic body. The angles in between are mainly determined by two ratios, namely E_1/E_3 and G_{13}/E_3 , where E_1 is the Young's modulus in the plane of transversely isotropy, E_3 is the Young's modulus perpendicular to the plane of transversely isotropy, and G_{13} is the shear modulus in the plane perpendicular to the plane of transversely isotropy (Amadei 1996). Under plane stress condition, the stress orientation can be formulated in terms of strain components as (Ramsay and Lisle 2000)

$$\tan 2\theta_\sigma = \frac{2m\left(1 - \frac{v_{13}^2}{n}\right)\gamma_{xy}}{(ne_x - e_y) - v_{13}(e_x - e_y)} \quad (1)$$



(a)



(b)

Fig. 14 The α angle of principal tensile strain at different loading stages with respect to 60° loading angle. **a** loading-displacement curve, **b** α angle at different stages

where θ_σ is the angle between the maximum principal stress and the plane of isotropy (parallel to the x -axis), v_{13} is the Poisson's ratio equals the contraction in the y -axis (normal to the plane of isotropy) as a proportion of extension in the x -axis (in the plane of isotropy), e_x , e_y , and γ_{xy} are plane strain components, $n = E_1/E_3$, and $m = G_{13}/E_3$.

It is assumed that the principal compressive stress is always parallel to the longer side of the sample during loading process, the deviation of principal strains from principal stresses can then be characterized by the α angle between principal tensile strain and horizontal direction. Variation of this angle during loading is exemplified by two cases, $\beta = 30^\circ$ and $\beta = 60^\circ$, as shown in Figs. 13 and 14. Similar variation trend of the non-coaxiality between principal strains and principal stresses can be seen from both cases. The

Table 2 Numerical simulation schemes and parameters

Simulation	E_1 (GPa)	E_3 (GPa)	E_1/E_3	ν_{12}	ν_{13}	G_{13} (GPa)
1	30	25	1.2	0.18	0.25	5
2	30	20	1.5	0.18	0.25	5
3	30	15	2.0	0.18	0.25	5
4	30	10	3.0	0.18	0.25	5
5	30	6	5.0	0.18	0.25	5
6	30	5	6.0	0.18	0.25	5

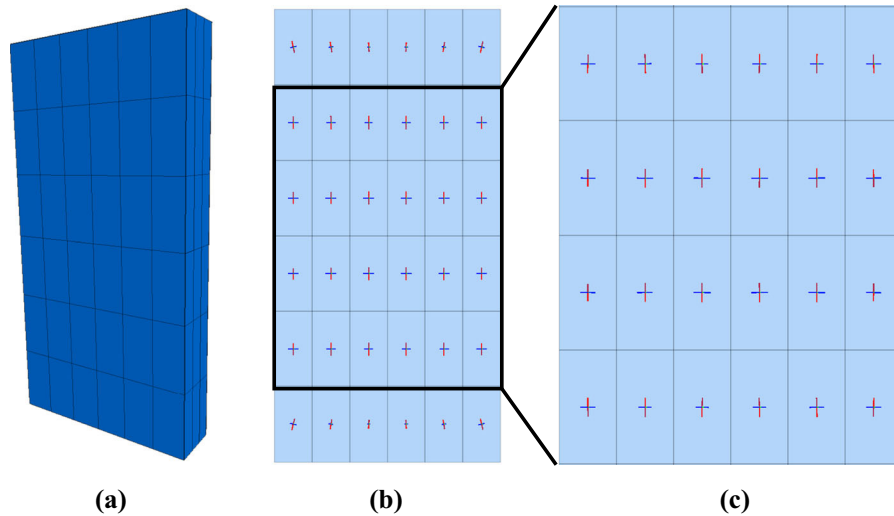
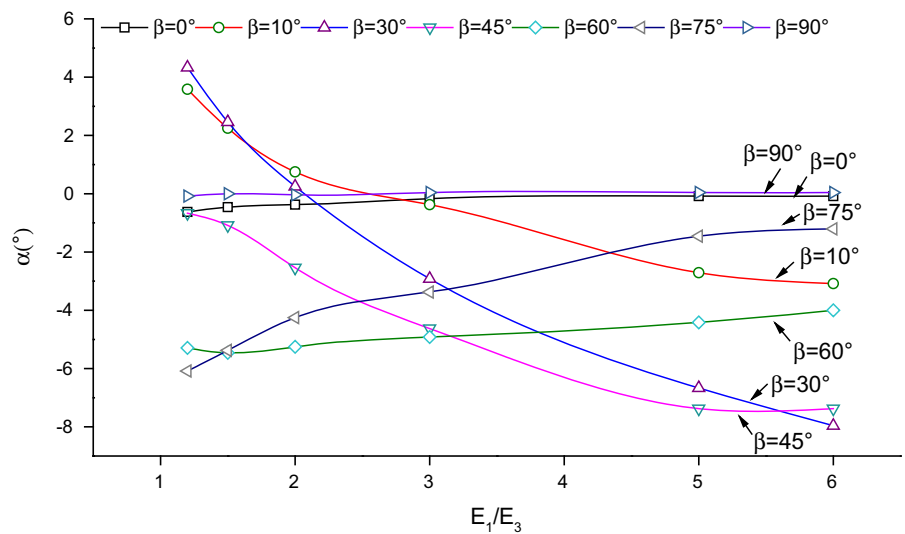
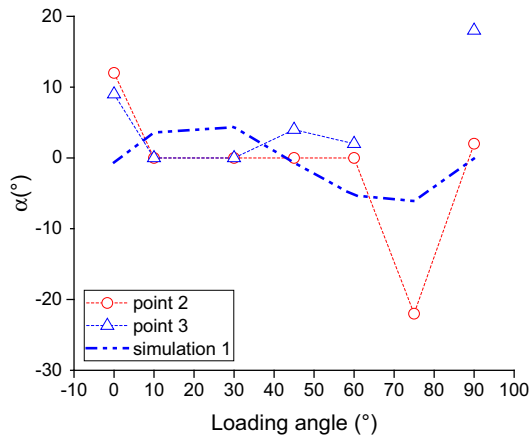


Fig. 15 Tensor representation of the principal strain rate calculated by FLAC^{3D}. **a** model discretization, **b** principal strain rate in the front 36 elements, **c** magnification of the 24

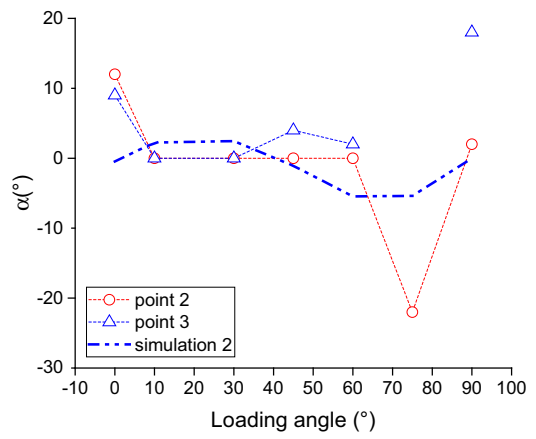
elements in the middle of the model. Red line represents minimum principal strain rate (compression), while blue line represents maximum principal strain rate (tension)

Fig. 16 Variation of α angle of principal tensile strain with the ratio of E_1/E_3 for different loading angles (β) by simulation

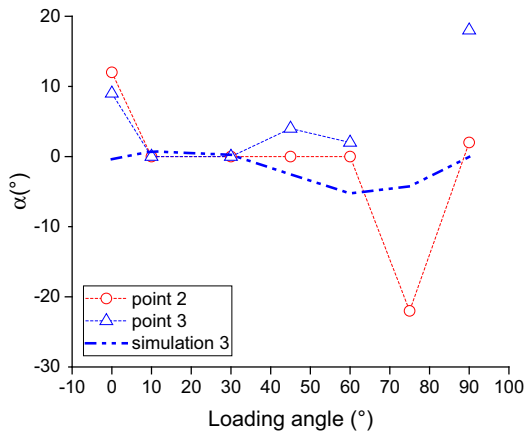




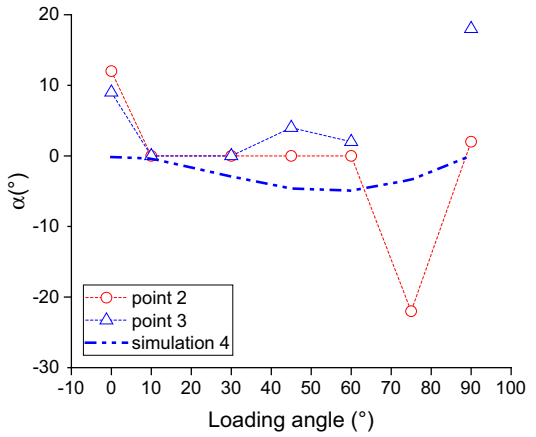
(a)



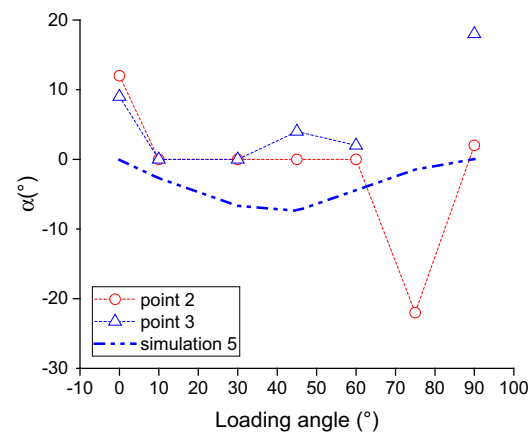
(b)



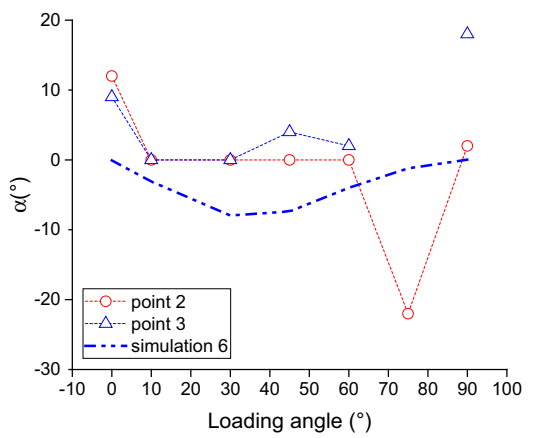
(c)



(d)



(e)



(f)

◀ **Fig. 17** Variation of α angle of principal tensile strain with loading angle for different simulations, compared with test results at elastic deformation stage. **a** $E_1/E_3 = 1.2$, **b** $E_1/E_3 = 1.5$, **c** $E_1/E_3 = 2.0$, **d** $E_1/E_3 = 3.0$, **e** $E_1/E_3 = 5.0$, **f** $E_1/E_3 = 6.0$

principal strain axes gradually approach the corresponding principal stress axes, from the initial disordered state to the ordered state, nearly coaxial (ideally coaxial or remains a small angle) state at peak strength. This has once again supported previous inference that the directions of principal strains are doubly affected by stress level and inherent anisotropy, while the former is more significant near peak strength.

4.3 Reconsideration of the Assumption of Transversely Isotropic

It is generally accepted that the layered rocks can be reasonably regarded as transversely isotropic body. By numerical simulation the non-coaxiality between principal strains and principal stresses can also be obtained if the transversely isotropic constitutive model is adopted. Thus the assumption of transversely isotropy can be verified by comparing testing results and numerical predictions. Furthermore the availability of transversely isotropy to the layered rocks can also be investigated accordingly. A total of 6 parameter groups are listed in Table 2 in which E_1/E_3 varies from 1.2 to 6.0. The commercial code FLAC^{3D} is used as simulation tool. The dimensions of the whole model are the same as the tested samples. The model is discretized into 108 hexahedron elements (Fig. 15). The embedded anisotropic elastic model (equivalent to transverse isotropic elastic model) is adopted, in which the dip direction and dip angle of the plane of transverse isotropy can be varied under the global geodetic coordinate system. A velocity of 2.5×10^{-8} m per step is assigned to both ends of the model in order to simulate the uniaxial compression. Figure 15 also shows the tensor representation of the principal strain rate in each element, in which the red line represents the minimum principal strain rate corresponding to compressive strain, while the blue line represents the maximum principal strain rate

corresponding to tensile strain under uniaxial compression. In order to minimize the influence of end effect, the results in the 12 elements comprising the upper and lower ends are neglected and only the middle 24 elements (4 rows by 6 columns, see Fig. 15c) are taken into account. The α angle of the principal tensile strain is the average value of the total 24 elements. All the values are recorded at the moment when the tensor direction exhibits negligible variation.

Three variation trends of the α angle can be identified from simulation, namely the increasing trend ($\beta = 60^\circ$ and 75°), the decreasing trend ($\beta = 10^\circ$, 30° and 45°), and almost steady trend ($\beta = 0^\circ$ and 90°), when the ratio of E_1/E_3 increases, as shown in Fig. 16. The overall range of α angle is -8° to 5° , while E_1/E_3 increases from 1.2 to 6. The α angle under $\beta = 0^\circ$ and 90° cases fluctuates around 0° , which indicates that the principal tensile strain is nearly perpendicular to the compression direction in both cases, while in other cases that strain forms a small angle (less than 10°) to the compressive stress. Moreover, there seem to be opposite trends between the two cases with complementary angles, such as $\beta = 30^\circ$ and 60° , or $\beta = 10^\circ$ (15° will be more obvious) and 75° . In fact, this is mainly attributed to the tensor transformation rule of the compliance tensor in the two cases with complementary angles. The positive correlation between α and E_1/E_3 can thus change into negative correlation if the loading angles are complementary. This perhaps also provides an explanation to the pattern transition around $\beta = 45^\circ$ or 60° described in Sect. 3.3.

The variations of α angle with loading angle β are shown in Fig. 17, together with the α angles measured at the middle sampling points 2 and 3 (Fig. 11) for different loading angles within elastic deformation stage. Comparison between experiment and simulation indicates that the simulated α angles with respect to each loading angle gradually deviate from those obtained by DIC analysis with the increase in E_1/E_3 . Simulation 2 or 3 appears to get the results closest to the tests in all the 6 simulations. Certain deviations ($\pm 20^\circ$) between test and simulation are found in both $\beta = 0^\circ$ and 75° cases, however, the general agreement suggests that the assumption of transverse isotropy is reasonable regarding the uncertainty in experiments.

5 Conclusions

In this paper, the main focus is put on investigating the full-field deformation characteristics of a bedded limestone using DIC technique. Two main aspects, namely the loading angle effect on the displacement field, and the evolution of displacement and strain fields during loading are discussed in detail. Conclusions can be drawn as follows:

1. Displacement fields at different loading stages exhibits two basic features, namely progressive rotation and from disordered to ordered deformation pattern. The horizontal and vertical displacement fields both rotate a large angle in comparison with their initial states while approaching peak strength. End effect is more obvious under specific occasions in which the principal strain axes near the upper and lower ends of a sample rotate relatively large angles with reference to the exact horizontal or vertical directions. At a specific moment during loading, the displacement and strain distributions on the sample surface are generally non-uniform.
2. The displacement pattern transits with loading angle. If the exact loading angle is smaller or larger than a threshold, the contour maps of displacements are different. While at the elastic deformation stage, this threshold for horizontal displacement is roughly 45° , whereas that for vertical displacement is roughly 60° .
3. The non-coaxiality between principal strains and stresses varies with loading process. The principal strain axes deviate rather obviously from the corresponding principal stress axes at initial loading and gradually change into coincidence while approaching peak strength. The angles between principal tensile strain and horizontal direction is within $\pm 20^\circ$. The principal tensile strains in the middle of a sample are nearly horizontal at elastic deformation stage when the loading angles change from 10° to 60° . The effect of stress level is more pronounced near peak strength which may conceal the influence of inherent anisotropy.

Acknowledgements This study is financially supported by the Chinese Natural Science Foundation with the Grant Nos. 51709043 and 41320104005.

References

- Alam SY, Loukili A, Grondin F et al (2015) Use of the digital image correlation and acoustic emission technique to study the effect of structural size on cracking of reinforced concrete. *Eng Fract Mech* 143:17–31
- Amadei B (1996) Importance of anisotropy when estimating and measuring in situ stresses in rock. *Int J Rock Mech Min Sci Geomech Abstr* 33(3):293–325
- Berfield TA, Patel JK, Shimmin RG et al (2007) Micro-and nanoscale deformation measurement of surface and internal planes via digital image correlation. *Exp Mech* 47(1):51–62
- Blaber J, Adair B, Antoniou A (2015) Ncorr: open-source 2D digital image correlation matlab software. *Exp Mech* 55(6):1105–1122
- Chang S, Wang CS, Xiong CY et al (2005) Nanoscale in-plane displacement evaluation by AFM scanning and digital image correlation processing. *Nanotechnology* 16(4):344
- Cho JW, Kim H, Jeon S et al (2012) Deformation and strength anisotropy of Asan gneiss, Boryeong shale, and Yeoncheon schist. *Int J Rock Mech Min Sci* 50:158–169
- Choi S, Shah SP (1997) Measurement of deformations on concrete subjected to compression using image correlation. *Exp Mech* 37(3):307–313
- Corr D, Accardi M, Graham-Brady L et al (2007) Digital image correlation analysis of interfacial debonding properties and fracture behavior in concrete. *Eng Fract Mech* 74(1–2):109–121
- Dai X, Yang F, Wang L et al (2013) Load capacity evaluated from fracture initiation and onset of rapid propagation for cast iron by digital image correlation. *Opt Lasers Eng* 51(9):1092–1101
- Dautriat J, Bornert M, Gland N et al (2011) Localized deformation induced by heterogeneities in porous carbonate analysed by multi-scale digital image correlation. *Tectonophysics* 503(1–2):100–116
- Dutton M, Take WA, Hoult NA (2013) Curvature monitoring of beams using digital image correlation. *J Bridge Eng* 19(3):05013001
- Fjær E, Nes OM (2014) The impact of heterogeneity on the anisotropic strength of an outcrop shale. *Rock Mech Rock Eng* 47(5):1603–1611
- Hakala M, Kuula H, Hudson JA (2007) Estimating the transversely isotropic elastic intact rock properties for in situ stress measurement data reduction: a case study of the Olkiluoto mica gneiss, Finland. *Int J Rock Mech Min Sci* 44(1):14–46
- Hoult NA, Take WA, Lee C et al (2013) Experimental accuracy of two dimensional strain measurements using digital image correlation. *Eng Struct* 46:718–726
- Lee C, Take WA, Hoult NA (2011) Optimum accuracy of two-dimensional strain measurements using digital image correlation. *J Comput Civ Eng* 26(6):795–803
- Lenoir N, Bornert M, Desrues J et al (2007) Volumetric digital image correlation applied to X-ray microtomography images from triaxial compression tests on argillaceous rock. *Strain* 43(3):193–205
- Leplay P, Réthoré J, Meille S et al (2011) Identification of damage and cracking behaviours based on energy

- dissipation mode analysis in a quasi-brittle material using digital image correlation. *Int J Fract* 171(1):35
- Li D, Zhu Q, Zhou Z et al (2017) Fracture analysis of marble specimens with a hole under uniaxial compression by digital image correlation. *Eng Fract Mech* 183:109–124
- Lin Q, Labuz JF (2013) Fracture of sandstone characterized by digital image correlation. *Int J Rock Mech Min Sci* 60:235–245
- Louis L, Wong TF, Baud P (2007) Imaging strain localization by X-ray radiography and digital image correlation: deformation bands in Rothbach sandstone. *J Struct Geol* 29(1):129–140
- Ma SP, Yan D, Wang X et al (2011) Damage observation and analysis of a rock Brazilian disc using high-speed DIC method. *Appl Mech Mater* 70:87–92
- McLamore R, Gray KE (1967) The mechanical behavior of anisotropic sedimentary rocks. *J Eng Ind* 89(1):62–73
- Munoz H, Taheri A, Chanda EK (2016) Pre-peak and post-peak rock strain characteristics during uniaxial compression by 3D digital image correlation. *Rock Mech Rock Eng* 49(7):2541–2554
- Nguyen TL, Hall SA, Vacher P et al (2011) Fracture mechanisms in soft rock: identification and quantification of evolving displacement discontinuities by extended digital image correlation. *Tectonophysics* 503(1–2):117–128
- Pan B, Qian K, Xie H et al (2009) Two-dimensional digital image correlation for in-plane displacement and strain measurement: a review. *Meas Sci Technol* 20(6):062001
- Ramsay JG, Lisle R (2000) *The Techniques of modern structural geology. Applications of continuum mechanics in structural geology, vol 3*. Academic Press, London, pp 777–778
- Schreier HW, Sutton MA (2002) Systematic errors in digital image correlation due to undermatched subset shape functions. *Exp Mech* 42(3):303–310
- Song H, Zhang H, Fu D et al (2013a) Experimental study on damage evolution of rock under uniform and concentrated loading conditions using digital image correlation. *Fatigue Fract Eng Mater Struct* 36(8):760–768
- Song H, Zhang H, Kang Y et al (2013b) Damage evolution study of sandstone by cyclic uniaxial test and digital image correlation. *Tectonophysics* 608:1343–1348
- Stirling RA, Simpson DJ, Davie CT (2013) The application of digital image correlation to Brazilian testing of sandstone. *Int J Rock Mech Min Sci* 60:1–11
- Sutton MA, Yan JH, Tiwari V et al (2008) The effect of out-of-plane motion on 2D and 3D digital image correlation measurements. *Opt Lasers Eng* 46(10):746–757
- Sutton MA, Orteu JJ, Schreier H (2009) *Image correlation for shape, motion and deformation measurements: basic concepts, theory and applications*. Springer, Berlin
- Tan X, Konietzky H, Frühwirth T et al (2015) Brazilian tests on transversely isotropic rocks: laboratory testing and numerical simulations. *Rock Mech Rock Eng* 48(4):1341–1351
- Tavallali A, Vervoort A (2010) Effect of layer orientation on the failure of layered sandstone under Brazilian test conditions. *Int J Rock Mech Min Sci* 47(2):313–322
- Tudisco E, Hall SA, Charalampidou EM et al (2015) Full-field measurements of strain localisation in sandstone by neutron tomography and 3D-volumetric digital image correlation. *Phys Procedia* 69:509–515
- Wattrisse B, Chrysochoos A, Muracciole JM et al (2001) Analysis of strain localization during tensile tests by digital image correlation. *Exp Mech* 41(1):29–39
- Wu ZM, Rong H, Zheng JJ et al (2011) An experimental investigation on the FPZ properties in concrete using digital image correlation technique. *Eng Fract Mech* 78(17):2978–2990
- Zhang H, Huang G, Song H et al (2012) Experimental investigation of deformation and failure mechanisms in rock under indentation by digital image correlation. *Eng Fract Mech* 96:667–675
- Zhou YY, Feng XT, Xu DP et al (2016) Experimental investigation of the mechanical behavior of bedded rocks and its implication for high sidewall caverns. *Rock Mech Rock Eng* 49(9):3643–3669

Publisher's Note Springer Nature remains neutral with regard to jurisdictional claims in published maps and institutional affiliations.